Int. J. Electron. Commun. (AEÜ) 159 (2023) 154451

Contents lists available at ScienceDirect

Int. J. Electron. Commun. (AEÜ)

journal homepage: www.elsevier.com/locate/aeue

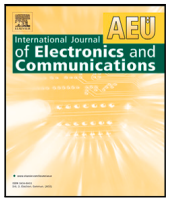

Regular paper

RF choke based methodology for flange effect mitigation and antenna isolation improvement in bistatic radars of aerospace vehicles

Rajender Daggula [a,b,*], Vasudeva Bevara [b], Manisha Kamal K. [b], Samba Siva Rao Kumbha [b], Amit Acharyya [a]

[a] Department of Electrical Engineering, IIT Hyderabad, Hyderabad, 502285, India
[b] Research Centre Imarat, Defence Research and Development Organization, Hyderabad, 500069, India

ARTICLE INFO

Keywords:
Choke flange
Bistatic radar
Radar cross section
Slot arrays
Traveling wave antennas

ABSTRACT

This paper presents a novel technique for mitigation of flange effect and antenna transmit to receive isolation improvement methodology using RF choke for the bistatic radars of aerospace vehicles. The presence of flange causes variation in antenna radiation pattern, by an increase in sidelobe level, decrease in gain and dip in roll pattern, thereby degradation in the performance of the antenna. An RF choke adjacent to the waveguide wall is introduced to nullify the undesirable effects of the flange. This Paper demonstrates through simulation and experimentation that this choke effectively suppresses the surface wave and can be applied in many types of antennas to improve the radiation pattern deteriorated by parasitic elements. It is also demonstrated through measurements that the isolation from transmit to receive antenna is improved by introducing choke, with this technique antenna isolation is enhanced by 23 dB with 11 dB antenna gain. The gain and sidelobe improvement of the antenna with RF choke is 2 dB, and 6 dB, respectively. The proposed array antenna is fabricated with and without choke, measurements are performed and test results are presented. The isolation test between transmit & receive antenna is performed in an anechoic chamber and test results are presented.

1. Introduction

Slotted Waveguide Array (SWA) antennas are frequently used in aerospace applications due to their inherent properties of high power handling, high temperature withstanding, linear polarization with minimum polarization conversion component, very low loss, and flush mount property. Kapoor et al. [1]; Chaturvedi et al. [2]. To achieve the communication distance requirement and mitigate path loss, high-efficiency and high-gain array antennas are also required. The computer numerical control (CNC) milling technology is a suitable fabrication technology when compared with the other planar works [3–5] because of the low loss, electrical discharge machining and slotted waveguide components are used in the antenna design to avoid dielectric and transmission losses [6].

For high-capacity short-range communication, the challenge is to provide interference suppression between two closely separated array antennas. As a result, the decoupling structure has a coplanar topology and is positioned on the common ground plane. It is possible to suppress the surface wave that exists on the common ground plane. In the past various authors worked theoretically and experimentally to determine the effects of the flange on radiation patterns, and proposed various structures like, rubber ferrite sheet [7], HIGP (High Impedance Ground Plane) [8], and Electromagnetic BandGap (EBG) structure [9] to mitigate these flange effects. Other researchers improved bistatic antenna isolation techniques by using EBG structures [10–13], Defected Ground Structure (DGS) [14–16], the Split-Ring Resonator (SRR) [17–20], and the isolated structure are some of the mutual coupling reduction techniques used, but these techniques are common in Multiple Input Multiple Output (MIMO) systems [21].

The main objective of the algorithm is to synthesize the physical parameters of the antenna to meet the required electrical parameters like Gain, Sidelobe level and Beamwidth.

The physical parameters are:
1. Length of the antenna.
2. Width ‘a’ and Height ‘b’ dimension of the waveguide
3. Number of Slots
4. Slot offset from waveguide center.
5. Slot length.

- Depending on the operating and cutoff frequencies, the width ‘a’ dimension is obtained.

* Corresponding author at: Research Centre Imarat, Defence Research and Development Organization, Hyderabad, 500069, India.
E-mail addresses: ee14resch11014@iith.ac.in (R. Daggula), vasudeva_b@srmap.edu.in (V. Bevara), manishakonda1995@gmail.com (Manisha Kamal K.), amit_acharyya@iith.ac.in (A. Acharyya).

https://doi.org/10.1016/j.aeue.2022.154451
Received 18 July 2022; Accepted 22 October 2022
Available online 7 November 2022

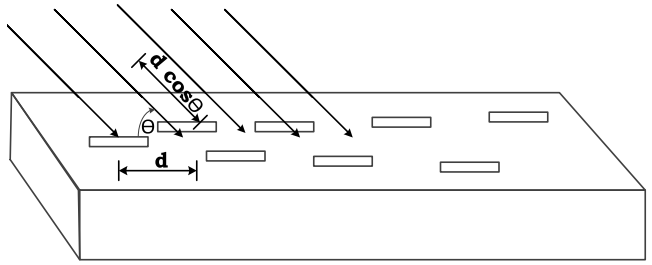

Fig. 1. Uniform Linear Array depicting phase contribution by various components.

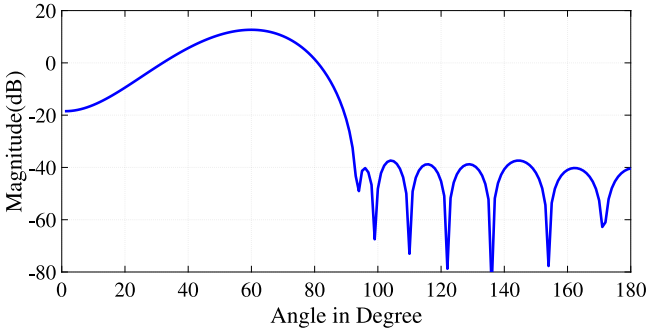

Fig. 2. Array factor by taking phase components and number of Elements into account.

- Height of the antenna is chosen to be half of the width of the antenna.
- Depending on the main beam pointing angle, guided wavelength is calculated.
- The no.of slots are calculated depending on the gain required.
- The inter element spacing is chosen to be $\frac{\lambda_g}{2}$, hence the total length of the antenna is N×$\frac{\lambda_g}{2}$ + $\frac{\lambda_g}{4}$, $\frac{\lambda_g}{4}$ is required from short to center of the last slot.
- Selection of the window depending on the required sidelobe level and main beam width.
- From the window pattern the power to be radiated by each slot.
- From the power, required admittance of each slot is calculated.
- The admittance is a function of offset from the center line, slot offset is obtained from the slot characterization data.

In this Paper, RF choke-based topology for slotted waveguide array antennas is proposed, to eliminate the flange's negative effects and to improve antenna transmit to receive isolation by suppressing surface waves. The antenna contains eight radiating slots on rectangular waveguide with RF choke, and it is mounted on the airframe of the aerospace vehicles.

2. Array antenna design

In this section, the slotted waveguide array design methodology is discussed. The array design procedure starts with the electrical specifications of the antenna. The typical specifications required are beam pointing angle of 64^0 from array axis, with H-plane beam-width of 20^0, and side lobe level better than 20 dB.

In standing waveguide configuration the inter-element spacing is $\lambda_g/2$ and the beam will be broadside.

As the beam-pointing angle is not broadside and is offset from broadside hence traveling waveguide fed slotted antenna configuration is chosen. Controlling the phase at each element by proper selection of inter-element spacing d, and controlling the amplitude taper, the main beam can be placed at the desired angle.

2.1. Array factor and antenna dimensions

The array factor for N-element linear array is given by

$$AF(\theta) = \sum_{n=1}^{N} a_n e^{-jn\psi} \tag{1}$$

ψ is the total phase shift between successive elements, a_n is the amplitude distribution which defines the beam-width and side-lobe level of the radiation pattern.

The total phase (ψ) at each element is the contribution from three components as shown in Fig. 1. The first contributor is, the wave reaching an element needs to travel $dcos\theta$ more distance in free space as compared to the wave reaching its preceding element. The wave travels in free space with a phase constant of $k_0 = 2\pi/\lambda_0$, the phase is $k_0 dcos\theta$.

The second component is the wave traveling inside the waveguide, the wave travels inside the waveguide with a guided phase constant of $\beta = 2\pi/\lambda_g$, the phase is $\beta * d$. The third component is, as the elements are placed alternate from the Centerline, introduces 180^0 phase. Hence the total phase is given by:

$$\psi = k_0 dcos(\theta) + \beta d - \pi \tag{2}$$

The maxima of the array factor occurs at $\psi = 2m\pi$, where m is 0,1,2... the angle θ at which ψ satisfies the above conditions is called beam pointing angle. In this application, m is chosen to be 0.

$$\psi = k_0 dcos(\theta) + \beta d - \pi = 0 \tag{3}$$

By varying inter-element spacing d and guided wavelength λ_g, the beam pointing angle is varied.

$$cos(\theta_0) = \frac{\pi - \beta d}{k_0 d} = \frac{\lambda_0}{2d} - \frac{\lambda_0}{\lambda_g} \tag{4}$$

The main beam is located depending on the selection of inter-element spacing and guided wavelength.

The inter-element spacing must be chosen, in such a way that there should not be any grating lobes, by following the below condition, grating lobes are avoided.

$$d < \frac{\lambda}{1 + cos(\theta_0)} \tag{5}$$

Guided wavelength is decided by the 'a' dimension of the waveguide, according to the Eq. (6).

$$\frac{1}{\lambda_0^2} = \frac{1}{\lambda_c^2} + \frac{1}{\lambda_g^2} \tag{6}$$

In the Eq. (6) by varying $\lambda_c = 2a$ guided wavelength is varied, as λ_0 is constant. By proper selection of cutoff frequency and cutoff wavelength, the 'a' dimension of the waveguide is finalized.

The height of the waveguide is chosen to be b=a/4. Depending on the beam-width, the number of elements thereby the length of the aperture is finalized. With the above constraints, the waveguide dimensions are finalized.

The total array factor is modeled by taking amplitude distribution and total phase distribution into account and plotted as shown in Fig. 2. From the plot, it is concluded that the beam pointing angle and side lobe level requirement are satisfied.

2.2. Slot radiator characterization

The main element that contributes to the radiation of electromagnetic waves is the slot, fed by the waveguide. As shown in Fig. 3, there are various types of slots possible:

a. Longitudinal Shunt Slot
b. Transversal series slot
c. Inclined slot on broad wall
d. Inclined slot on narrow wall

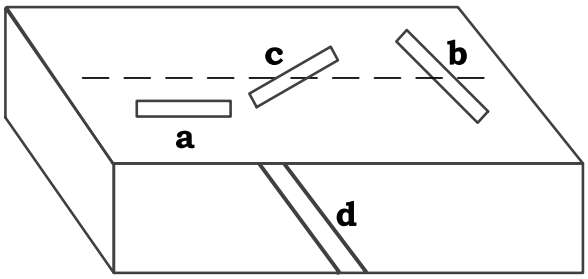

Fig. 3. Various types of possible slot configurations.

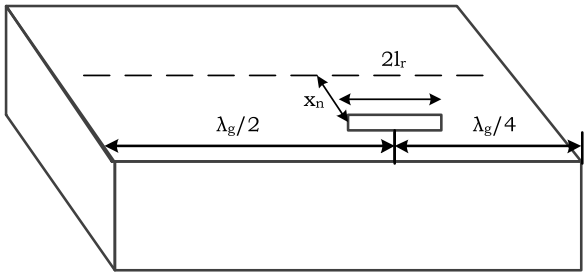

Fig. 4. Graphical representation with various dimensions of Slot.

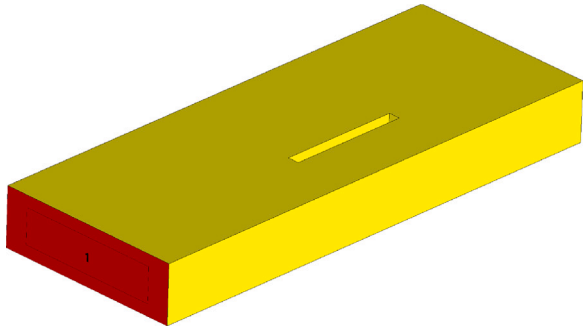

Fig. 5. CAD model of the representation of Slot.

Longitudinal shunt slot is chosen as the suitable candidate as a radiator, because of the low cross-polarization component as compared to inclined slots, and wide E-Plane beam-width as compared to the transversal series slot.

The next step after the selection of the appropriate slot is the characterization of the slot. In CST microwave studio slot CAD model is realized for characterization as shown in Fig. 4, the graphical representation is shown in Fig. 5. From the short-circuited wall end, the center of the slot is kept at $\lambda_g/4$, the short circuit acts as an open circuit at the center of the slot and it has no effect on the normalized admittance of the slot.

The measurement is made from a distance of $\lambda_g/2$ from the center of the slot because the admittance repeats for every $\lambda_g/2$ on the smith chart, thereby the slot admittance is measured.

The resonant slot length is the length of the slot where the admittance contains only conductance, and the susceptance part is zero.

$$\frac{Y}{G_0} = g(x)h(y) = \frac{-\tau}{1+\tau} \tag{7}$$

$$h(y) = h_1(y) + jh_2(y) \tag{8}$$

Where h_1 refers the normalized slot conductance, h_2 refers the normalized susceptance, τ is reflection coefficient and $y = \frac{l}{l_r}$ in Eqs. (7) and (8). For a given offset from the center, resonant length (l_r) of the slot is identified, the length of the slot (l) is varied by ±10% from the resonant length in CST, the reflection coefficient data is exported to MATLAB, and code is developed to extract normalized conductance(G) and susceptance(B) data and is plotted in Fig. 6. By varying the offset, resonant length and conductance values are noted and plotted in Fig. 7.

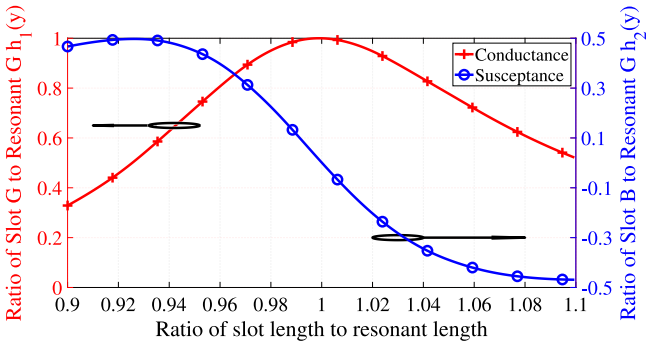

Fig. 6. Slot normalized conductance and susceptance with respect to length.

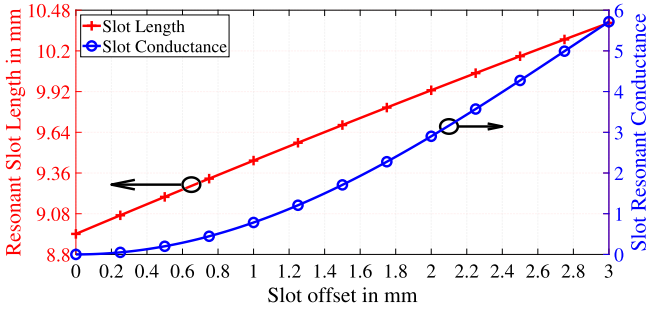

Fig. 7. Slot resonant conductance and length with respect to slot offset.

The equations for resonant length, normalized conductance in terms of offset, and slot length, normalized susceptance equations are developed using curve fitting techniques.

$$l_r(x_n) = -6.612x_n^2 + 13.07x_n + 8.941 \tag{9}$$

$$g(x_n) = 7.431 sin\frac{\pi x_n}{a}^2 \tag{10}$$

$$h_1(y) = 1 - 56(y-1)^2 \tag{11}$$

$$h_2(y) = -5.882(y-1) \tag{12}$$

From the Eqs. (9)–(12), As the offset from the centerline grows, the conductance of the slot increases, and thus the radiated power increases. To obtain the desired excitation, the conductance of the slots must be varied across the array, which involves adjusting the offset, and the resonant length must also be changed to achieve resonance. These equations are used to synthesize the traveling wave array.

2.3. Traveling wave array synthesis

As the beam pointing angle is away from the broadside, a traveling wave-fed array is chosen. Traveling wave array is realized by placing matched termination beyond the last slot. Elliott's design procedure [22] for traveling wave array design (Eq. (13)) is used for achieving the Taylor aperture distribution across the array.

$$h_2(y) = -5.882(y-1) \tag{13}$$

$$\left|\frac{Y_1^a}{G_0}\right| = \left|\frac{V_n^s}{V_1^s}\right|^2 \times \left|\frac{Y_n^a}{G_0}\right| \tag{14}$$

Table 1
Slot excitation, offsets and lengths.

Slot	Excitation	Slot offset(mm)	Resonant length(mm)
1	0.09	0.07	8.98
2	0.34	0.26	9.08
3	0.71	0.57	9.23
4	1.00	0.9	9.41
5	1.00	1.3	9.59
6	0 .71	1.74	9.81
7	0.34	2.36	10.1
8	0.09	3.95	10.8

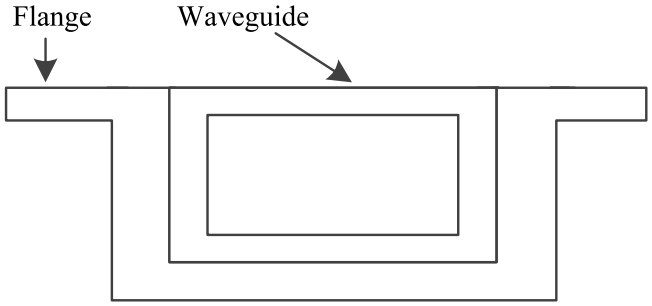

Fig. 8. Waveguide array antenna cross sectional view.

$\left|\frac{(Y_n^a)}{G_0}\right|$ is the normalized shunt admittance of nth slot. V_n^s is the excitation voltage on nth slot.

The normalized shunt admittance of all slots is detected using MATLAB code based on Eq. (14) in order to obtain the required excitation voltages.

The offsets and resonant lengths are determined using these shunt admittances, and an iterative technique is constructed to calculate mutual impedance between the slots and recalculate offsets and lengths until the desired aperture distribution is attained. Table 1 lists the estimated offsets and lengths, as well as the aperture distribution.

2.4. Choke design

Although the aforementioned antenna is just constructed with a rectangular waveguide, a flange is required to mount the antenna to the body of the aircraft vehicle, as shown in Fig. 8.

Due to the flow of the surface wave on the flange and diffraction of this wave from the edges, variations in slot conductance result in variations in aperture distribution, resulting in a drop in side-lobe level and gain of the H-Plane pattern.

The edge diffraction also causes constructive and destructive interference along E-Plane (Roll), causing a dip in the far-field pattern hence decrease in E-Plane beam-width.

The radiated fields from the slots are shown in Fig. 9. The radiated fields due to slots and surface currents are shown in Fig. 10.

The flow of surface waves on the flange causes the flange to act as a parasitic element and causes the deterioration of the antenna radiation pattern. Hence it is required to suppress this surface wave, it is done by creating an open circuit at the waveguide edge i.e. before starting the flange, as is waveguide without flange.

It is feasible by inserting a quarter-wave short-circuited transmission line between the waveguide and the flange, which operates as an open circuit as shown in Fig. 11.

The input impedance of a transmission line with a characteristic impedance (Z_0) and a load impedance (Z_l) can be calculated using the Eq. (15) shown in Fig. 12.

$$Z_{in} = Z_0 \frac{(Z_l \cosh(\gamma d) + Z_0 \sinh(\gamma l))}{(Z_0 \cosh(\gamma d) + Z_l \sinh(\gamma l))} \tag{15}$$

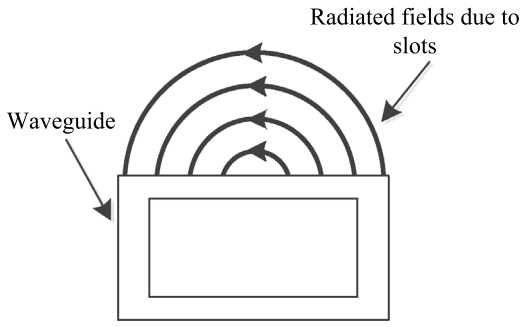

Fig. 9. Radiated Fields only due to slots.

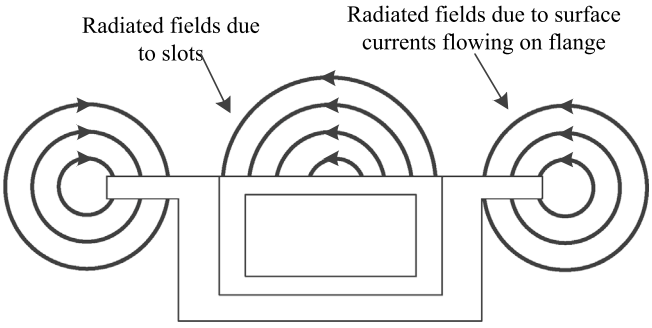

Fig. 10. Radiated Fields due to slots and surfaces.

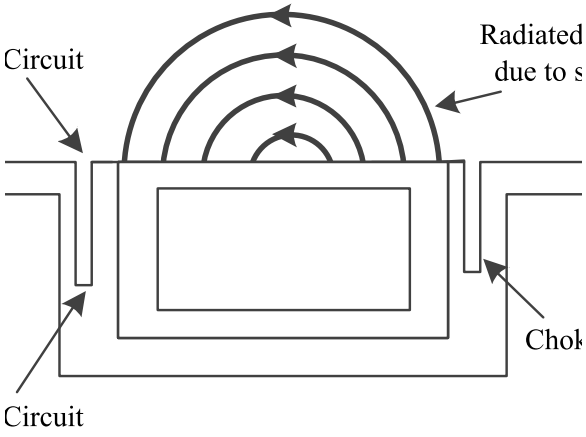

Fig. 11. Array antenna with flange and choke.

If Z_l is short circuit,

$$Z_{in} = Z_0 \tanh(\gamma l) \tag{16}$$

Here $l = \frac{\lambda}{4}$, $\gamma = \alpha + j * \beta$ For lossless line, $\alpha = 0, \beta = \frac{2\pi}{\lambda}$

$$\begin{aligned} Z_{in} &= Z_0 * \tanh\left(\frac{j\pi}{2}\right) \\ &= Z_0 * \tan\frac{\pi}{2} \\ &= \infty \end{aligned} \tag{17}$$

Thus, the open circuit can be introduced from a short-circuited quarter-wave transmission line. The same technique is used in the present work, an open circuit region is created at end of the waveguide wall by a short-circuited quarter-wavelength groove. Due to this electrical open circuit, the surface wave is obstructed, there is no diffraction of the wave at the edges and the radiation pattern is improved in H-plane as well as in E-Plane.

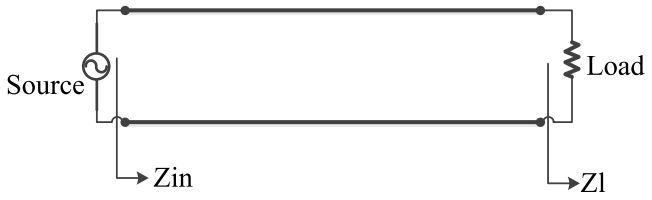

Fig. 12. Transmission line representation.

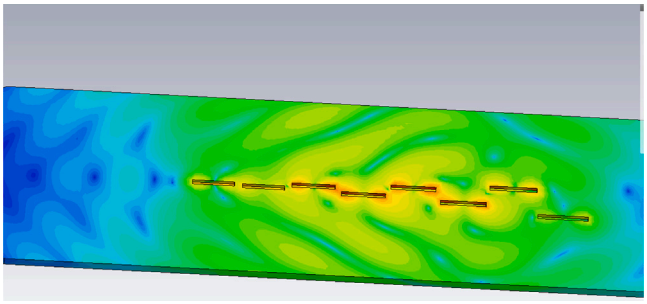

Fig. 13. Surface current distribution on antenna with flange.

Table 2
Gain and side-lobe level values of three antennas.

Antenna	Gain	Side lobe
Wave Guide	12.81 dB	−27.8 dB
With Flange	8.8 dB	−21.3 dB
With Choke	11.01 dB	−27.9 dB

3. Antenna with RF choke

After designing and modeling the rectangular slotted waveguide array antenna in MATLAB, a CAD model was created in CST software, and simulation studies were conducted. The outcomes are in line with the specifications.

The flange is added for mechanical integration of the antenna to the vehicle segment, and simulation studies were undertaken after the flange was introduced. The antenna gain is reduced, the side-lobe level deteriorates, and the E-Plane pattern shows undulation.

The surface current distribution of the Slotted waveguide antenna with flange is illustrated in Fig. 13. Surface currents can be observed flowing on the flange. The fluctuation in the antenna's radiation pattern is caused by these surface currents.

A choke is introduced to mitigate the aforementioned effect, as shown in Fig. 14(a) with a cross-sectional view and Fig. 14(b) with a top view. The simulation studies are carried out, and an improvement in the antenna's emission pattern is observed.

The Surface current distribution of the antenna with choke is shown in Fig. 15, it can be seen that there is no flow of surface currents on the flange. From this phenomenon, it is concluded that the choke is acting as open circuit for the currents, hence there is no flow of current on the flange.

The H-Plane simulated patterns of three antenna configurations: a simple rectangular waveguide antenna, the antenna with flange, and the antenna with choke & flange, are shown in Fig. 16. The gain of a rectangular antenna is reduced by 4 dB, and the sidelobe level is deteriorated by 6.3 dB after the introduction of the flange to a rectangular antenna. When compared to the flange arrangement, the gain is improved by 2.2 dB, and the sidelobe level is improved by 6.6 dB with the addition of the choke. Table 2 compares the three antenna designs.

Similarly, the E-Plane simulated patterns of three antennas are shown in Fig. 17. It can be observed from the plot that there is no dip at 0 angle in the rectangular antenna, a dip of 4 dB in the antenna following the introduction of the flange, and no dip and flattened roll pattern in the antenna with choke. Fields diffracted from both the edges of the flanges cause the dip in the radiation pattern.

Fig. 18 shows the antenna 3-D far-field simulated radiation pattern in CST. The beam is slanted by 64^0 from the antenna axis, and there is no dip in the roll plane, as can be observed from the radiation pattern.

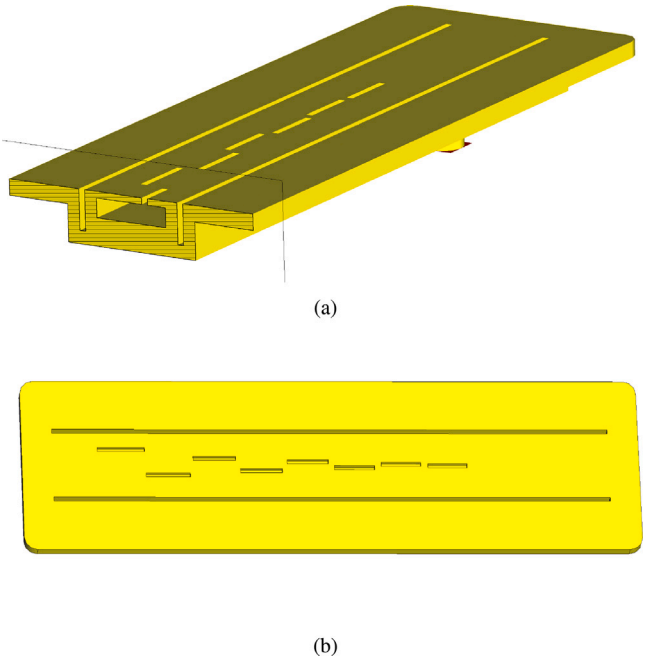

Fig. 14. (a) Cross sectional view of slotted waveguide array with choke (b) Top view of Antenna with choke.

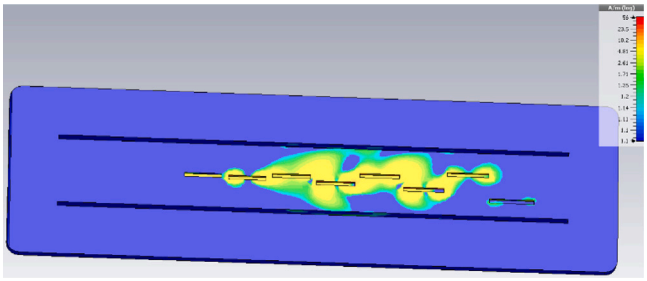

Fig. 15. Surface current distribution on antenna with choke.

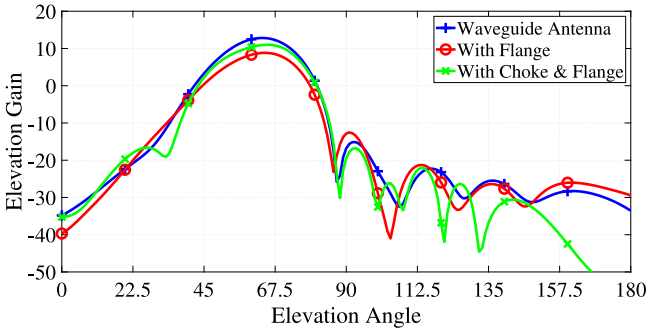

Fig. 16. H-Plane Radiation Pattern.

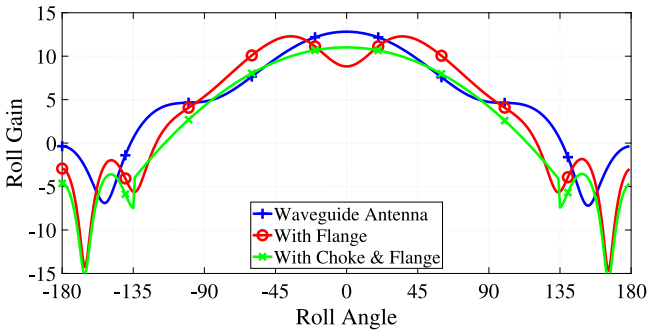

Fig. 17. E-Plane Radiation Pattern.

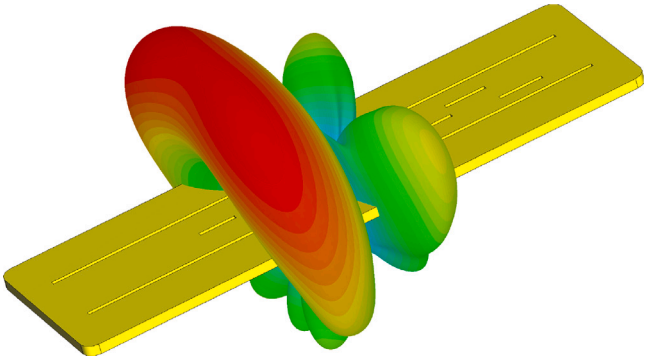

Fig. 18. Antenna 3D Far-field pattern.

Fig. 19. Fabricated SWA antenna.

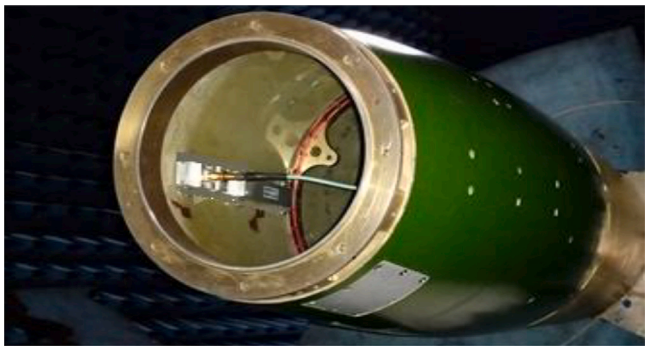

Fig. 20. Antenna measurement in anechoic chamber.

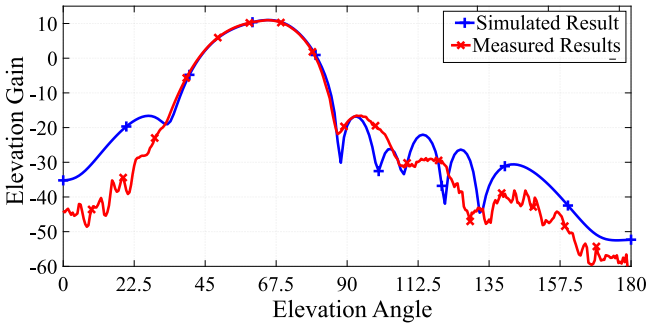

Fig. 21. Measured and Simulated radiation patterns of SWA Antenna.

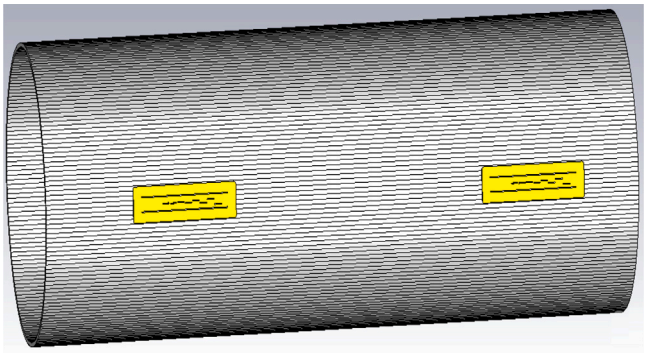

Fig. 22. Isolation measurement simulation setup for SWA Antenna.

4. Fabrication and measurement details

The Ku-band SWA antenna with the RF choke is fabricated by using the CNC milling technique as shown in Fig. 19. The fabricated slotted waveguide antenna with RF choke has a total dimension of 130mm × 22mm × 7mm.

The antenna measurements are carried out on an in-house compact antenna test range with the setup shown in Fig. 20. Measurements are performed in 0.5° angular increments with the antenna mounted in the section as it will be in the final arrangement. For gain computation, the antenna is kept in receive mode and the received power is compared to that of a typical gain antenna.

The radiation pattern of the fabricated antenna is measured and the results are shown in Fig. 21. The value obtained for beam tilt angle, gain, and beam width is all consistent with the measured values. Measurement performance at the sidelobe level is superior to simulated performance.

The isolation test is carried out in an anechoic chamber with an equipment setup. The signal is generated and fed to the transmit antenna from the signal generator, and a spectrum analyzer is linked to the receiving antenna as illustrated in Fig. 23. The difference between transmitted and received power levels demonstrates the isolation between transmit and receive antennas when using calibrated RF connections.

Isolation simulation investigations are carried out by placing a CAD model of two antennas on the portion illustrated in Fig. 22, and simulating the insertion loss between the two antenna ports.

The simulation shows that the isolation is 59 dB without the choke and 82 dB with the choke. With a choke, isolation improved by 23 dB.

The outcomes of this work are compared to earlier pattern enhancement strategies in Table 3. Although the structure is simple, it has achieved considerable improvements in gain, sidelobe level, and roll pattern form. Table 4 demonstrates that the isolation enhancement is compared to traditional technologies, the RF choke structure delivers the highest isolation of 23 dB.

Finally, the performance comparison between proposed and conventional prototypes [23–29] are tabulated in Table 4.

Fig. 23. Test Setup for SWA antenna.

Table 3
Comparison with reported radiation pattern improvement mechanisms.

	This Work	Wei et al. [30]	Li et al. [31]	Zhang and Yuan [32]
Technique	RF Choke	Comb-Shaped Choke	Electro-magnetic Band-Gap	HIGP
Gain improvement	2 dB	0.5 dB	2 dB	1.6 dB
SLL improvement	6 dB	4 dB	2 dB	6 dB

Table 4
Performance comparisons among different mechanisms.

S.No	Decoupling method	Antenna type	Isolation improve-ment (dB)	Fully integrated structure	Fabrica-tion technol-ogy
[23]	Meta surface	Quad-ridge horn	0–20	No	CNC
Manafi et al. [24]	Patch Array	Quad-ridge horn	15	No	PCB
Liang and Co [25]	Virtual Element	Microstrip Patch	9	Yes	NA
Ding et al. [26]	EBG	SIW Slotted	21	Yes	MMPT
Zhang et al. [27]	Envelop Shaping	Waveguide slot array	NA	No	DBLTCP
Yao et al. [28]	Choke Slot Array	Step-Profiled horn array	2–20	Yes	MEMS
Yang and Rahmat-Samii [29]	EBG	Microstrip Patch	8	Yes	NA
This Work	RF Choke	Slotted Waveguide	23	Yes	CNC

5. Conclusion

This paper proposed, the application of RF choke-based topology to reduce the flange effect and to enhance the isolation between transmitter and receiver antennas. The choke reduces the surface waves and improves the radiation properties of the SWA antenna, as demonstrated by FIT simulations and experiments. When compared to conventional methods, this technique improves gain by 2 dB and SLL by 4 dB. The isolation improvement achieved is 23 dB, the improvement is 8.69%, 60.8% and 65.2% as compared to other methods proposed in [25,26, 29] respectively. Other strategies are designed for each purpose, but this methodology enhances not only the pattern characteristics of the specific antenna but also the isolation qualities. This technology can be applied to a variety of applications where surface waves must be suppressed in order to get better performance metrics.

Declaration of competing interest

The authors declare the following financial interests/personal relationships which may be considered as potential competing interests: Rajender Daggula reports was provided by Research Centre Imarat.

Data availability

No data was used for the research described in the article.

References

[1] Kapoor A, Mishra R, Kumar P. Frequency selective surfaces as spatial filters: Fundamentals, analysis and applications. Alex Eng J 2022;61(6):4263–93.
[2] Chaturvedi D, Kumar A, Raghavan S. An integrated SIW cavity-backed slot antenna-triplexer. IEEE Antennas Wirel Propag Lett 2018;17(8):1557–60.
[3] Wu YF, Cheng YJ, Huang ZX. Ka-band near-field-focused 2-D steering antenna array with a focused rotman lens. IEEE Trans Antennas and Propagation 2018;66(10):5204–13.
[4] Wu YF, Cheng YJ. Proactive conformal antenna array for near-field beam focusing and steering based on curved substrate integrated waveguide. IEEE Trans Antennas and Propagation 2019;67(4):2354–63.
[5] Wang HB, Cheng YJ. Single-layer dual-band linear-to-circular polarization converter with wide axial ratio bandwidth and different polarization modes. IEEE Trans Antennas and Propagation 2019;67(6):4296–301.
[6] Ferrando-Rocher M, Herranz-Herruzo JI, Valero-Nogueira A, Bernardo-Clemente B. Performance assessment of gap-waveguide array antennas: CNC milling versus three-dimensional printing. IEEE Antennas Wirel Propag Lett 2018;17(11):2056–60.
[7] Chakraborty T, Sharma S, Debnath T, Mahapatra AS, Selvam A, Chakrabarti S, et al. Fabrication of heterostructure composites of Ni-Zn-Cu-ferrite-C3N4-poly (vinylidene fluoride) films for the enhancement of electromagnetic interference shielding effectiveness. Chem Eng J 2021;420:127683.
[8] Sharma N, Bhatia SS. Ultra-wideband fractal antenna using rhombus shaped patch with stub loaded defected ground plane: Design and measurement. AEU-Int J Electron Commun 2021;131:153604.
[9] Lima AM, Cunha NHO, da Silva JP. Electromagnetic band gap based in peano fractal geometry for harmonic suppression. Microw Opt Technol Lett 2021;63(5):1360–5.
[10] Qiu L, Zhao F, Xiao K, Chai S-L, Mao J-J. Transmit–receive isolation improvement of antenna arrays by using EBG structures. IEEE Antennas Wirel Propag Lett 2012;11:93–6.
[11] Farahani HS, Veysi M, Kamyab M, Tadjalli A. Mutual coupling reduction in patch antenna arrays using a UC-EBG superstrate. IEEE Antennas Wirel Propag Lett 2010;9:57–9.
[12] Tan X, Wang W, Wu Y, Liu Y, Kishk AA. Enhancing isolation in dual-band meander-line multiple antenna by employing split EBG structure. IEEE Trans Antennas and Propagation 2019;67(4):2769–74.
[13] Modak S, Khan T. A slotted UWB-MIMO antenna with quadruple band-notch characteristics using mushroom EBG structure. AEU-Int J Electron Commun 2021;134:153673.
[14] Cheng Y-F, Ding X, Shao W, Wang B-Z. Reduction of mutual coupling between patch antennas using a polarization-conversion isolator. IEEE Antennas Wirel Propag Lett 2016;16:1257–60.
[15] Niu Z, Zhang H, Chen Q, Zhong T. Isolation enhancement in closely coupled dual-band MIMO patch antennas. IEEE Antennas Wirel Propag Lett 2019;18(8):1686–90.
[16] Mark R, Mishra N, Mandal K, Sarkar PP, Das S. Hexagonal ring fractal antenna with dumb bell shaped defected ground structure for multiband wireless applications. AEU-Int J Electron Commun 2018;94:42–50.
[17] Ameen M, Ahmad O, Chaudhary RK. Single split-ring resonator loaded self-decoupled dual-polarized MIMO antenna for mid-band 5G and C-band applications. AEU-Int J Electron Commun 2020;124:153336.
[18] Dadgarpour A, Zarghooni B, Virdee BS, Denidni TA, Kishk AA. Mutual coupling reduction in dielectric resonator antennas using metasurface shield for 60-GHz MIMO systems. IEEE Antennas Wirel Propag Lett 2016;16:477–80.
[19] Gupta S, Briqech Z, Sebak AR, Denidni TA. Mutual-coupling reduction using metasurface corrugations for 28 GHz MIMO applications. IEEE Antennas Wirel Propag Lett 2017;16:2763–6.

[20] Ghosh J, Mitra D, Das S. Mutual coupling reduction of slot antenna array by controlling surface wave propagation. IEEE Trans Antennas and Propagation 2018;67(2):1352–7.
[21] Pant A, Singh M, Parihar MS. A frequency reconfigurable/switchable MIMO antenna for LTE and early 5G applications. AEU-Int J Electron Commun 2021;131:153638.
[22] Elliott RS. Antenna theory and design. Wiley-IEEE Press; 2003.
[23] Pk PV, Elmansouri MA, Filipovic DS. Wideband decoupling techniques for dual-polarized bi-static simultaneous transmit and receive antenna subsystem. IEEE Trans Antennas and Propagation 2017;65(10):4991–5001.
[24] Manafi S, Al-Tarifi MA, Filipovic DS. Isolation improvement techniques for wideband millimeter-wave repeaters. IEEE Antennas Wirel Propag Lett 2018;17(2):355–8.
[25] Liang W, Co FAWC. Vehicle-mounted Millimeter-wave Radar. In: 2019 International applied computational electromagnetics society symposium - China, Vol. 1. Applied Computational Electromagnetics Society; 2019, p. 1–2.
[26] Ding M, Wang X, Tang L, Qu J, Wu R. A W-band antenna array based on SIW structure with enhanced gain and high isolation. In: 2019 Photonics electromagnetics research symposium - fall. 2019, p. 2290–5. http://dx.doi.org/10.1109/PIERS-Fall48861.2019.9021843.
[27] Zhang M, Hirokawa J, Ando M. A four-corner-fed double-layer waveguide slot array with low sidelobes developed for a 40 GHz-band DDD system. IEEE Trans Antennas and Propagation 2016;64(5):2005–10.
[28] Yao SS, Cheng YJ, Wu YF, Fan Y. Isolation enhancement for W-band coplanar array antennas based on silicon micromachining technology. IEEE Antennas Wirel Propag Lett 2020;19(10):1744–8.
[29] Yang F, Rahmat-Samii Y. Microstrip antennas integrated with electromagnetic band-gap (EBG) structures: A low mutual coupling design for array applications. IEEE Trans Antennas and Propagation 2003;51(10):2936–46. http://dx.doi.org/10.1109/TAP.2003.817983.
[30] Wei J, Chen ZN, Qing X, Shi J, Xu J. Compact substrate integrated waveguide slot antenna array with low back lobe. IEEE Antennas Wirel Propag Lett 2013;12:999–1002. http://dx.doi.org/10.1109/LAWP.2013.2277876.
[31] Li L, Dang XJ, Li B, Liang CH. Analysis and design of waveguide slot antenna array integrated with electromagnetic band-gap structures. IEEE Antennas Wirel Propag Lett 2006;5(4):111–5. http://dx.doi.org/10.1109/LAWP.2006.872438.
[32] Zhang G, Yuan N. Radiation characteristics improvement in waveguide-fed slot antenna with a high-impedance ground plane (HIGP). Microw Opt Technol Lett 2005;45(2):176–9. http://dx.doi.org/10.1002/mop.20762.